

This is the accepted manuscript made available via CHORUS. The article has been published as:

Emergence of asymmetric skew-scattering dominated
anomalous Nernst effect in the spin gapless
semiconductors

$\text{Co}_{1-x}\text{Fe}_x$
 CrGa

A. Chanda, Deepika Rani, Jadupati Nag, Aftab Alam, K. G. Suresh, M. H. Phan, and H. Srikanth

Phys. Rev. B **106**, 134416 — Published 18 October 2022

DOI: [10.1103/PhysRevB.106.134416](https://doi.org/10.1103/PhysRevB.106.134416)

1 **Emergence of asymmetric skew-scattering dominated anomalous Nernst**
2 **effect in spin gapless semiconductors $\text{Co}_{1+x}\text{Fe}_{1-x}\text{CrGa}$**

3
4 A. Chanda¹, Deepika Rani,^{2#} Jadupati Nag², Aftab Alam², K. G. Suresh^{2*}, M. H. Phan,^{1*} and
5 H. Srikanth^{1*}

6 ¹ *Department of Physics, University of South Florida, Tampa FL 33620*

7 ² *Magnetic Materials Laboratory, Department of Physics, Indian Institute of*
8 *Technology Bombay, Mumbai - 400076, India*

9 [#]*Presently at Indian Institute of Technology Delhi, New Delhi - 110016*

10 **Corresponding authors: suresh@phy.iitb.ac.in; phanm@usf.edu; sharihar@usf.edu*

11 **Keywords:** spin gapless semiconductors, Heusler alloys, anomalous Nernst effect, skew
12 scattering

13 **Abstract**

14 Heusler alloy-based spin gapless semiconductors (SGSs) with very high Curie temperatures
15 (T_C) have recently gained enormous attention because of their unconventional electronic
16 structures. They exhibit a non-zero band gap in one of the spin channels and a zero band gap
17 in the other spin channel, making them an important class of materials for tunable spin transport.
18 Here, we report the first ever experimental observation of anomalous Nernst effect (ANE) in
19 $\text{Co}_{1+x}\text{Fe}_{1-x}\text{CrGa}$ ($x = 0, 0.2, 0.4, \text{ and } 0.5$), which are the emerging quaternary Heusler alloy-
20 based SGSs. While the electron-electron elastic scattering and the disorder mediated weak
21 localization effect play the major roles in electrical transport for all the samples at low
22 temperatures, the magnon-drag effect was found to dominate the longitudinal thermoelectric
23 transport. The ANE coefficient at room temperature increases from $\approx 0.018 \mu\text{V} \cdot \text{K}^{-1}$ for $x = 0$
24 to $\approx 0.063 \mu\text{V} \cdot \text{K}^{-1}$ for $x = 0.5$, which is higher than that for $\text{Ni}_{81}\text{Fe}_{19}$ and compressively

1 strained SrRuO₃ films. Our analysis indicates that the observed ANE in these samples
2 originates from asymmetric skew-scattering of charge carriers.

3

1 **1. Introduction**

2 Recent progress in the field of spin caloritronics has stimulated renewal of interest in efficiently
3 harvesting electrical energy from waste thermal energy by exploiting the spin degree of
4 freedom of the charge carriers in a magnetic conductor [1]. The anomalous Nernst effect (ANE)
5 is one of such emerging magneto-thermoelectric phenomena, wherein an electrical field (\vec{E}_{ANE})
6 is generated in a ferromagnetic conductor transverse to the directions of both applied
7 temperature gradient ($\vec{\nabla T}$) and the magnetization (\vec{M}), and can be expressed as, $\vec{E}_{ANE} =$
8 $Q_{ANE}(\mu_0 \vec{M} \times \vec{\nabla T})$, where Q_{ANE} is the coefficient of ANE [2,3]. Berry curvature at the Fermi
9 level associated with the Bloch waves in the reciprocal space (\vec{k} space) has been identified as
10 the underlying intrinsic origin of large room temperature ANE coefficient observed in a range
11 of topological magnetic materials *e.g.*, the full-Heusler ferromagnet Co_2MnGa ($\sim 6 \mu\text{V. K}^{-1}$) [4],
12 magnetic Weyl semimetal $\text{Co}_3\text{Sn}_2\text{S}_2$ ($\sim 5 \mu\text{V. K}^{-1}$) [5,6], iron-based cubic ferromagnets Fe_3Ga
13 ($\sim 4 \mu\text{V. K}^{-1}$) and Fe_3Al ($\sim 2 \mu\text{V. K}^{-1}$) [7], kagome ferromagnets Fe_3Sn ($\sim 3 \mu\text{V. K}^{-1}$) [8] and
14 Fe_3Sn_2 ($\sim 1.26 \mu\text{V. K}^{-1}$) [9], chiral antiferromagnet Mn_3Sn ($\sim 0.35 \mu\text{V. K}^{-1}$) [2], *etc.*, as well as
15 gigantic low temperature ANE coefficient in correlated non-centrosymmetric kagome
16 ferromagnet $\text{UCo}_{0.8}\text{Ru}_{0.2}\text{Al}$ ($\sim 23 \mu\text{V. K}^{-1}$) [10], canted antiferromagnet YbMnBi_2 ($\sim 6 \mu\text{V. K}^{-1}$) [11], van der Waals ferromagnet Fe_3GeTe_2 ($\sim 0.3 \mu\text{V. K}^{-1}$) [12], *etc.* Apart from the intrinsic
17 mechanisms, extrinsic mechanisms such as, asymmetric skew scattering can also give rise to
18 large ANE coefficient especially in magnetic oxides *e.g.*, Fe_3O_4 single crystals [13], hole-
19 doped manganite $\text{La}_{1-x}\text{Na}_x\text{MnO}_3$ [14], ferromagnetic cobaltites [15–17], *etc.*

21

22 Recently, spin gapless semiconductors (SGSs) have attracted immense attention of the
23 spintronics community due to their unconventional electronic structures; while they exhibit a
24 finite band gap for one spin channel, the conduction and valence band edges touch for the other

1 spin channel [18]. Thus they possess the characteristics of both half-metallic ferromagnets and
2 gapless semiconductors. Because of such unique feature of their band structure, their transport
3 properties are extremely susceptible to external stimuli, *e.g.*, temperature and magnetic field
4 which in combination with their high spin polarization make them potential tunable spintronic
5 materials. Although the SGS behavior was originally predicted in diluted magnetic
6 semiconductors (DMS), Heusler alloys-based SGS materials appear to be more advantageous
7 than the DMS-based SGSs because of their high Curie temperature (T_C) and sizable spin
8 polarization [19–22]. In addition to the well-studied topological Heusler alloy Co_2MnGa , the
9 ANE has been extensively investigated in plenty of full Heusler compounds *e.g.*, Co_2TiSn [23],
10 $\text{Ni}_{46.5}\text{Co}_2\text{Mn}_{37}\text{Sn}_{14.5}$ [24], $\text{Co}_2\text{Fe}_{0.4}\text{Mn}_{0.6}\text{Si}$ [25], Co_2MnSi [26], $\text{Co}_2\text{MnAl}_{1-x}\text{Si}_x$ [27],
11 Ni_2MnGa [28], etc. However, to our knowledge, ANE in Heusler alloy-based SGS materials
12 has not been explored so far.

13

14 The quaternary Heusler alloys $\text{Co}_{1+x}\text{Fe}_{1-x}\text{CrGa}$ with very high Curie temperature ($T_C \geq$
15 690 K) were found to exhibit extraordinary SGS behaviour for $x \leq 0.4$ but become completely
16 half-metallic for $x = 0.5$ [22,29]. Here, we have performed a comprehensive investigation of
17 ANE in $\text{Co}_{1+x}\text{Fe}_{1-x}\text{CrGa}$ as a function of magnetic field and temperature. We found that the
18 electron-electron elastic scattering and the weak localization effect play the dominant roles in
19 electrical transport for all the samples at low temperatures and the contributions from these
20 scatterings increase considerably with x for $x \leq 0.4$. On the other hand, the magnon-drag effect
21 was found to dominate the longitudinal thermoelectric transport in all the samples. Our study
22 indicates that the ANE coefficient increases gradually with x for $x \leq 0.4$ but has a drastic
23 increase for $x = 0.5$, when the system transforms from the SGS state to the completely half-
24 metallic state. An in-depth analysis of the temperature dependence of transverse thermoelectric
25 coefficient (S_{xy}), longitudinal Seebeck coefficient (S_{xx}) and the longitudinal resistivity (ρ_{xx})

1 indicates that the observed ANE in these samples originates from the skew-scattering
2 mechanism.

3

4 **2. Experimental**

5 Polycrystalline samples of $\text{Co}_{1-x}\text{Fe}_x\text{CrGa}$ were synthesized by arc melting technique.
6 The synthesis method and the crystal phase characterization of these samples are reported
7 elsewhere [22,29]. The crystal structure of these samples were determined by X-ray diffraction
8 (XRD) pattern at room temperature using Xpert pro diffractometer with Cu-K α radiation ($\lambda =$
9 1.54184 Å). Static magnetic characterization of the samples was performed using a vibrating
10 sample magnetometer (VSM) attached to a commercial physical property measurement system
11 (PPMS) from Quantum Design. Electrical resistivity (ρ_{xx}) measurements on these samples
12 were performed using the DC resistivity option of the PPMS. Longitudinal thermopower (S_{xx})
13 measurements on these samples were carried out using a home-made sample stage for the
14 PPMS. ANE on these samples were measured as a function of temperature and magnetic field
15 using a custom-built spin caloritronic measurement set up by making use of a universal sample
16 puck for the PPMS. The samples were sandwiched between two copper blocks (hot and cold).
17 The bottom (hot) block was thermally detached from the PPMS puck base by a 4-mm thick
18 Teflon block to retain a temperature difference of ~ 10 K between the PPMS puck base and the
19 hot block. On the other hand, the top (cold) block was thermally connected to the PPMS puck
20 base by a pair of molybdenum screws. To maintain a stable temperature difference between
21 these two blocks, temperatures of both these blocks were controlled using PID temperature
22 controllers (Scientific Instruments 9700). Temperature gradient was applied between these two
23 blocks using two Pt100 RTD sensors (used as resistive heaters) attached to both these blocks.
24 A calibrated Si-diode thermometer was attached to each of these blocks that accurately
25 recorded the temperatures T_{hot} and T_{cold} corresponding to temperatures of the hot and cold

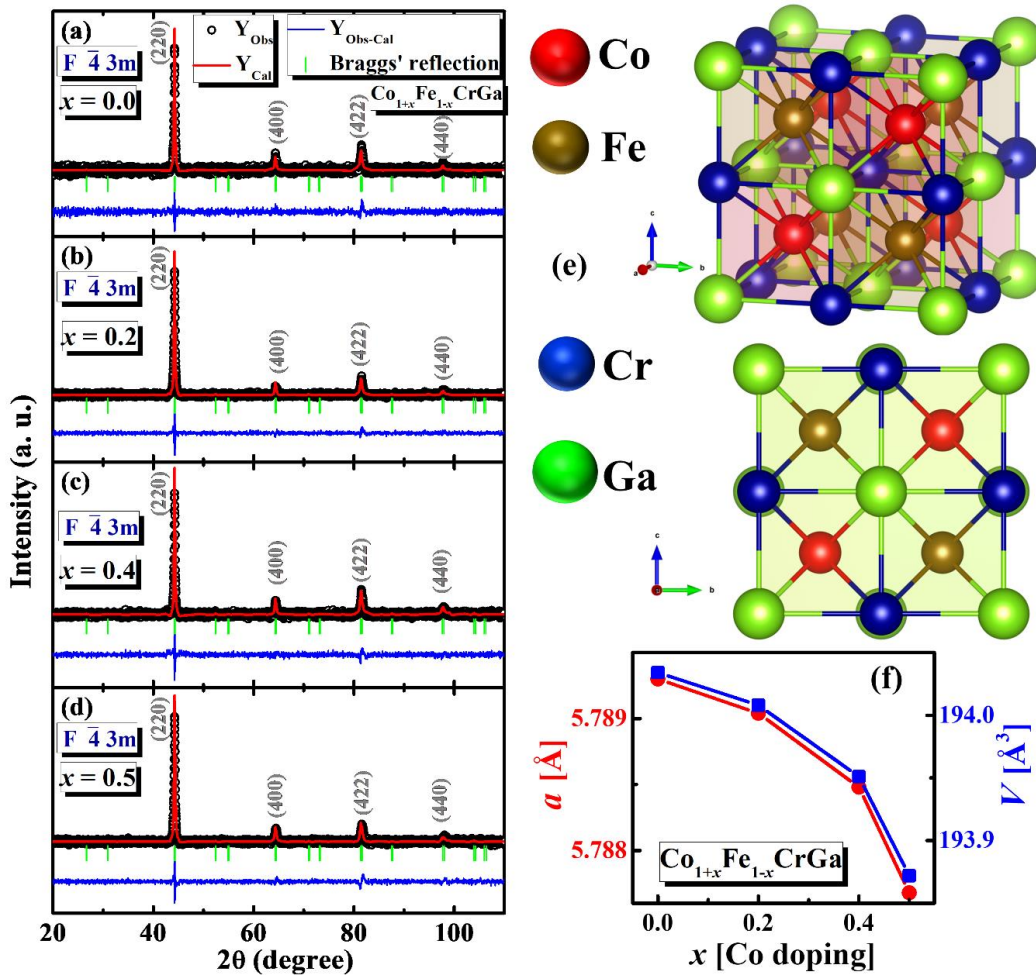
1 blocks, respectively. The sample temperature was recorded as the average temperature,
2 $T_{sample} = \frac{T_{hot} + T_{cold}}{2}$. In order to electrically insulate the sample surfaces from the copper
3 blocks, a thin layer of kapton tape was thermally anchored to the bare surfaces of both the
4 copper blocks. Note that the kapton tape acts as a good thermal conductor and poor electrical
5 conductor. Additionally, cryogenic Apiezon N-grease was applied to the kapton tapes attached
6 to the surfaces of both these blocks to ensure good thermal connectivity between the sample
7 surfaces and the copper blocks. Moreover, both the temperature sensors were attached to the
8 closest proximity of the sample surface in order to accurately read the temperatures of the hot
9 and cold ends of the sample. A more detailed description of our experimental set up is reported
10 elsewhere [30,31]. Note that the applied temperature difference between the hot and cold plates
11 is primarily dropped across the sample and the influence of interfacial thermal resistances can
12 be neglected, as discussed in the Supplemental Material [32–35]. The transverse thermoelectric
13 voltage generated due to the ANE was measured using a Keithley 2182A nanovoltmeter, while
14 scanning a DC magnetic field produced by the superconducting magnet of the PPMS. We used
15 the same set up for temperature dependence of longitudinal Seebeck coefficient measurement.
16 During the measurement at any specific temperature, a temperature gradient was applied
17 between the hot and cold plates once the desired sample temperature was reached. Once a stable
18 temperature difference between the hot and cold plates, ΔT was attained, the thermally
19 generated voltage across the sample along the direction of temperature gradient was recorded.
20 The background voltage and other spurious contributions were eliminated by reversing the
21 direction of temperature gradient and averaging the thermally generated voltages.

22

23 **3. Results and Discussion**

24 **Figure 1**(a)-(d) demonstrate the room temperature X-ray diffraction (XRD) patterns for the
25 samples $x = 0.0, 0.2, 0.4$ and 0.5 , respectively along with the Rietveld analysis performed using

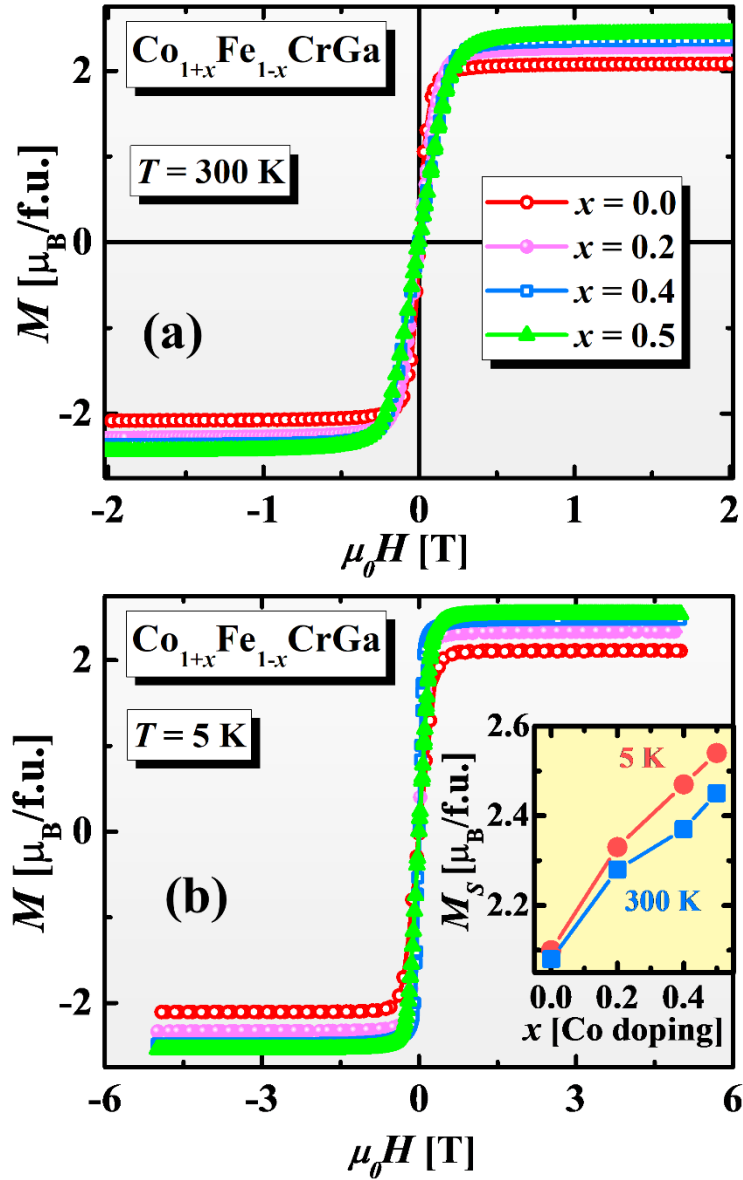
1 the Fullprof Suite software. The observed Bragg reflections indicate that these alloys adopt
 2 cubic crystal structure with space group $F\bar{4}3m$ having the structural prototype of LiMgPdSn.
 3 Using synchrotron-based XRD measurements, our previous report [29] indicated the existence
 4 of the low-angle superlattices reflections (111) and (200) peaks, which are not visible in the
 5 standard XRD patterns and hence, partially rules out the possibility of the presence of B2 and
 6 A2 type antisite disorders. On the other hand, an earlier report on Mössbauer spectroscopy
 7 performed on the pristine CoFeCrGa alloy confirmed the presence of DO₃ type disorder [22].
 8 We believe that a certain amount of DO₃ type antisite disorder is present in all our samples [29].



9
 10 **Figure 1.** X-ray diffraction (XRD) patterns for the samples (a) $x = 0.0$, (b) $x = 0.2$, (c) $x = 0.4$
 11 and (d) $x = 0.5$, respectively in $\text{Co}_{1+x}\text{Fe}_{1-x}\text{CrGa}$ along with the Rietveld analysis. (e) Schematic
 12 illustration of the crystal structure of CoFeCrGa . (f) Variation of lattice parameter (left y-scale)
 13 and unit cell volume (right y-scale) with x .

1 A schematic representation of the crystal structure of CoFeCrGa is shown in Fig. 1(e), where
 2 Ga, Cr, Fe and Co atoms occupy the Wyckoff positions of 4a, 4b, 4c, and 4d considering type
 3 I structure [36]. The lattice parameter (a) and unit cell volume (V) were evaluated from the
 4 Rietveld analysis. As shown in Fig. 1(f), both a and V decrease gradually with increasing Co
 5 content, which is in agreement with the previous study [29].

6



7

8 **Figure 2.** Magnetic field dependence of magnetization, $M(H)$ for $\text{Co}_{1+x}\text{Fe}_{1-x}\text{CrGa}$ at (a) $T =$
 9 300 K and (b) 5 K, inset of (b) shows x -dependence of saturation magnetization, M_s .

10

1 **Figure 2**(a) and (b) display the magnetic field dependence of magnetization, $M(H)$
2 measured at $T = 300$ and 5 K on the Heusler alloy series $\text{Co}_{1-x}\text{Fe}_{1-x}\text{CrGa}$ with $x = 0.0, 0.2, 0.4$
3 and 0.5 . $M(H)$ for all the samples exhibit negligible hysteresis at both the temperatures,
4 indicating the soft-magnetic nature of the samples. Most importantly, the saturation
5 magnetization, M_S of the samples increases monotonically with x at both the temperatures as
6 shown in the inset of **Fig. 2**(b). The experimental values of M_S at $T = 5$ K for $x = 0, 0.2, 0.4$ and
7 0.5 are $2.1, 2.33, 2.47$ and $2.54\mu_B/\text{f. u.}$, respectively, which are close to those estimated using
8 the Slater-Pauling rule [37]. An earlier report shows that the magnetic transition temperature
9 (T_C) of these samples are very high and it increases linearly from 686 K for $x = 0$ to 870 K for
10 $x = 0.5$ [29]. **Figure 3**(a) and (b) represent the T -dependence of longitudinal resistivity, $\rho_{xx}(T)$
11 for the samples $x = 0$ and 0.5 . While $\rho_{xx}(T)$ for $x = 0$ exhibits semiconducting behavior
12 ($\frac{\partial\rho_{xx}}{\partial T} < 0$) throughout the measured temperature range, that for $x = 0.5$ shows metallic-like
13 resistivity ($\frac{\partial\rho_{xx}}{\partial T} > 0$) from room temperature down to 50 K at which it shows a minimum in
14 ρ_{xx} followed by a remarkable upturn below $T^* \approx 50$ K [29]. A closer inspection reveals that
15 $\rho_{xx}(T)$ for $x = 0$ also shows a weak slope-change around $T^* = 50$ K (indicated by an arrow)
16 below which ρ_{xx} increases at a faster rate with decreasing temperature. Note that $\rho_{xx}(T)$ for
17 samples $x = 0.2$ and 0.4 also exhibit semiconducting behavior throughout the measured
18 temperature range with more pronounced slope changes at $T^* \approx 50$ K in comparison to $x = 0$
19 followed by enhanced $\left|\frac{\partial\rho_{xx}}{\partial T}\right|$ below $T^* \approx 50$ K. The relative change in ρ_{xx} below $T^* \approx 50$ K,
20 $\frac{\Delta\rho_{xx}}{\rho_{xx}} = \frac{\rho_{xx}(T=10\text{ K}) - \rho_{xx}(T=50\text{ K})}{\rho_{xx}(T=50\text{ K})}$ increases from ≈ 0.05 for $x = 0$ to ≈ 0.1 for $x = 0.4$.

21
22 We start with the analysis of the $\rho_{xx}(T)$ data taking into consideration different bulk
23 scattering mechanisms. Generally, the electrical resistivity of a conducting material can be
24 expressed as: $\rho_{xx} = \rho_{xx}^{\text{elastic}} + \rho_{xx}^{\text{inelastic}}$ [38]. Here, $\rho_{xx}^{\text{elastic}}$ represents the contribution

1 from electron-electron elastic scattering due to the Coulomb interaction between conduction
 2 electrons, which usually has a $T^{1/2}$ (*i.e.*, $\rho_{xx}^{elastic} = \rho_e T^{1/2}$) and dominates at low- T [39]. It is
 3 believed that the resistivity minimum accompanied by a low- T upturn can arise from elastic
 4 electron-electron interaction when the low-temperature resistivity exceeds the Mott's
 5 maximum limit of metallic resistivity of ≈ 10 m Ω . cm [38,39], which is much higher than the
 6 low- T value of ρ_{xx} (≈ 0.32 m Ω . cm at 10 K for $x = 0$) for our samples. However, in a highly
 7 disordered 3D metal such as our $\text{Co}_{1+x}\text{Fe}_{1-x}\text{CrGa}$ system [29], the weak localization effect
 8 (WLE) [39] arising from the disorder mediated coherent backscattering of charge carriers can
 9 also give rise to the low- T upturn in resistivity and it has the T -dependence of $\sim T^{-1/2}$ [39–41].
 10 On the other hand, the Kondo-like [42] transport arising from the interaction between localized
 11 magnetic moments associated with magnetic impurities and the mobile electrons can also give
 12 rise to the low- T upturn in resistivity in a disordered magnetic material and it has the T -
 13 dependence of $\sim \ln T$ [39,43,44]. As shown in **Fig. S1**, [32] we fitted the $\rho_{xx}(T)$ data with the
 14 WLE and Kondo effect separately in the low- T region and found that the WLE can describe
 15 the upturn more effectively. Therefore, the rapid upturn in $\rho_{xx}(T)$ for $x = 0.5$ as well as the
 16 low- T slope change followed by enhanced $\left| \frac{\partial \rho_{xx}}{\partial T} \right|$ for $x = 0-0.4$ below T^* possibly originate from
 17 the WLE [29]. On the other hand, $\rho_{xx}^{inelastic}$ signifies the contributions from different inelastic
 18 scattering mechanisms, such as, electron-electron (ρ_{el-el}), electron-phonon (ρ_{el-ph}),
 19 electron-magnon (ρ_{el-mag}), double-magnon (ρ_{mag}) scatterings in magnetic conductors [35].
 20 Here, the electron-electron scattering contribution arises due to inelastic collision between light
 21 (s -electrons) and heavy electrons (d -electrons) and usually varies as T^2 [46,47]. The
 22 contribution from the scattering of conduction electrons by lattice phonons follows T^5 -
 23 behavior [44,45] at low- T but, shows a T -linear behavior at high- T [48]. The contribution of
 24 electron-magnon scattering towards resistivity also follows T^2 -dependence [45]. However, in

1 case of half metals, [49,50] the T^2 -dependent electron-magnon scattering contribution
 2 exponentially decays due to the gapped spin-flip scattering and the contribution from electron-
 3 magnon scattering becomes, [50,51] $\rho_{e-m}(T) \propto T^2 e^{-(T/\Delta)}$; where, $k_B\Delta$ is the spin wave
 4 energy gap which accounts for the difference between the Fermi level and the nearest band
 5 edge of unoccupied minority spins [50], and k_B is the Boltzmann constant. Nevertheless, there
 6 is an energy gap between the filled conduction and unoccupied valence band edges associated
 7 with the minority spin channel for both half metals and spin gapless semiconductors [19,29].
 8 Therefore, the aforementioned electron-magnon scattering model is valid for both the systems.
 9 It is also noteworthy that the contribution of the electron-electron inelastic scattering is
 10 insignificant compared to the other contributions [45]. Therefore, we have neglected the
 11 contribution of the electron-electron inelastic scattering towards $\rho_{xx}(T)$ for our $\text{Co}_{1+x}\text{Fe}_{1-x}\text{CrGa}$
 12 system. We found that the $\rho_{xx}(T)$ data for all our samples was found to fit well with the
 13 expression: $\rho_{xx}(T) = \rho_0 + \rho_e T^{1/2} + \rho_{WLE} T^{-1/2} + \rho_{el-ph} T^5$ in the low- T (below the up-
 14 turn) region and with the expression: $\rho_{xx}(T) = \rho'_0 + \rho_{el-mag} T^2 e^{-(T/\Delta)} + \rho_{el-ph} T$ in the
 15 high- T (above the up-turn) region. Notably, for the low temperature region, we excluded the
 16 electron-magnon scattering term as the electron-electron elastic scattering and weak
 17 localization are the most significant and dominating mechanisms for the resistivity up-turn at
 18 low temperatures. Here, ρ_0 and ρ'_0 are the residual resistivity arising from the scattering of
 19 conduction electrons by lattice defects and impurities respectively [38,52].
 20

21 The variations of the fitting parameters with Co doping are depicted in **Fig. S3**. [32]
 22 For the high temperature fits, the absolute values of ρ_{el-mag} and Δ increase with x for $x \leq 0.4$,
 23 but decrease considerably for $x = 0.5$. It is also evident that both ρ_{el-ph} and ρ_{el-mag} are
 24 negative for $x \leq 0.4$ which is expected as ρ_{xx} for these samples decreases with increasing
 25 temperature. However, the absolute value of ρ_{el-ph} does not vary significantly with x for $x \leq$

1 0.4, but changes its sign for $x = 0.5$ for which $\rho_{xx}(T)$ shows metallic-like behavior above the
2 up-turn. The obtained values of Δ for our $\text{Co}_{1+x}\text{Fe}_{1-x}\text{CrGa}$ system are higher than those reported
3 for the well-known half metallic CrO_2 ($\Delta \approx 80$ K), [51] Fe_2Si ($\Delta \approx 85$ K), [49] and Co_2FeSi
4 ($\Delta \approx 100$ K), [50] etc. However, the value of Δ is lower in the sample $x = 0.5$ (half metal)
5 compared to the samples $x \leq 0.4$ (spin gapless semiconductors) in our $\text{Co}_{1+x}\text{Fe}_{1-x}\text{CrGa}$ system.
6 On the other hand, it is apparent that the absolute values of ρ_e and ρ_{WLE} in the low temperature
7 region increase with x for $x \leq 0.4$, but decrease for $x = 0.5$. Clearly, ρ_e is negative for all the
8 samples which is expected at low temperatures. Negative temperature coefficient for the
9 electron-electron scattering is reported in different Heusler alloys [41,53] as well as disordered
10 manganites [52] showing low temperature resistivity up-turns. However, ρ_{el-ph} decreases
11 slightly with x for $x \leq 0.4$ but increases for $x = 0.5$. Nevertheless, the absolute value of ρ_{el-ph}
12 is extremely small compared to that of ρ_e and ρ_{WLE} for all the samples indicating that the
13 electron-electron elastic scattering and WLE play the dominant roles in electrical transport for
14 all the samples at low temperatures.

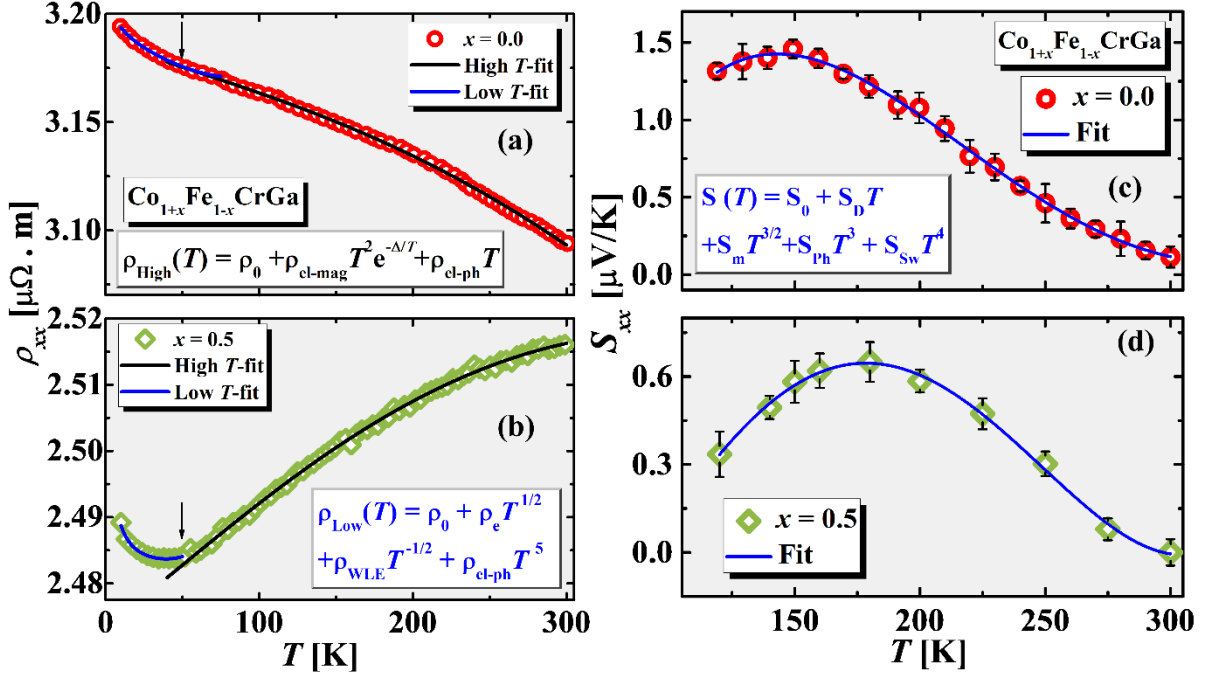
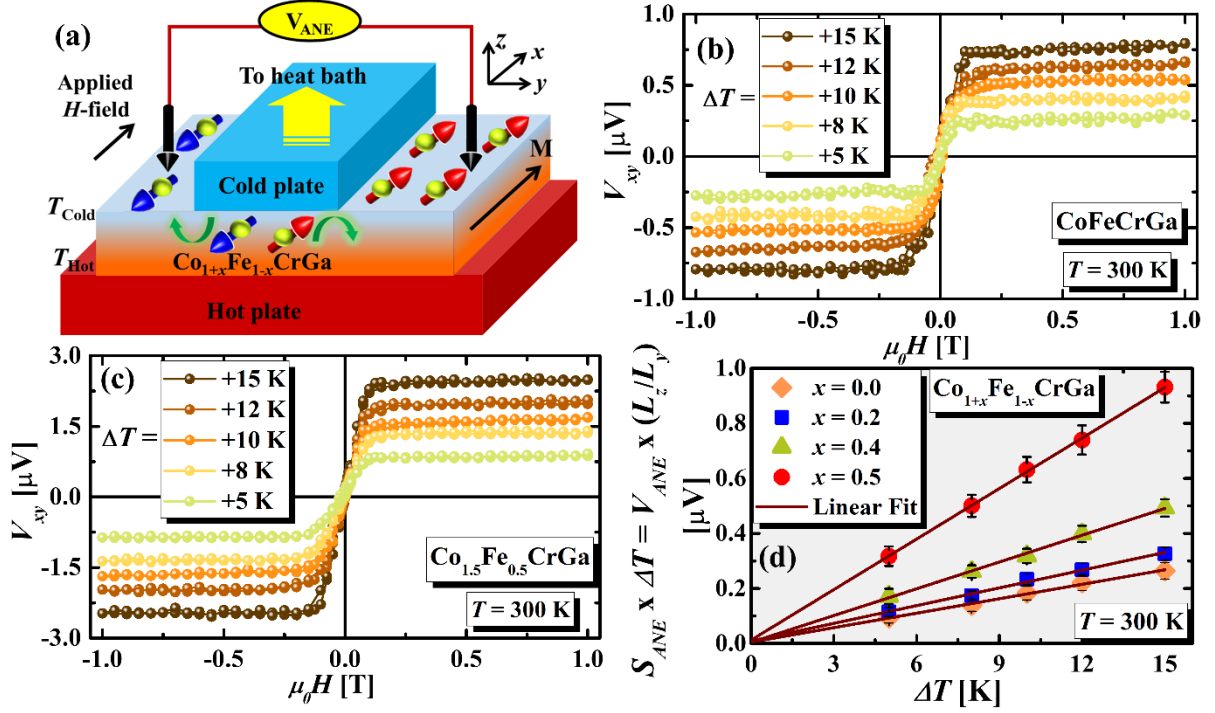


Figure 3. Temperature dependence of longitudinal resistivity, $\rho_{xx}(T)$ for (a) $x = 0.0$ and (b) $x = 0.5$ in $\text{Co}_{1+x}\text{Fe}_{1-x}\text{CrGa}$, fitted with $\rho_{xx}(T) = \rho'_0 + \rho_{el-mag}T^2 e^{-(T/\Delta)} + \rho_{el-ph}T$ in the high temperature region and with $\rho_{xx}(T) = \rho_0 + \rho_e T^{1/2} + \rho_{WLE} T^{-1/2} + \rho_{el-ph} T^5$ in the low temperature region. Temperature dependence of longitudinal Seebeck coefficient, $S_{xx}(T)$ for (c) $x = 0.0$ and (d) $x = 0.5$ fitted with $S_{xx}(T) = S_0 + S_d T + S_{mag} T^{3/2} + S_{ph} T^3 + S_{sw} T^4$.

Next, we focus on the thermoelectric transport in our $\text{Co}_{1+x}\text{Fe}_{1-x}\text{CrGa}$ system. **Figure 3(c)** and **(d)** represent the T -dependence of longitudinal thermopower, $S_{xx}(T)$ for the samples $x = 0.0$ and 0.5 . The sign of $S_{xx}(T)$ for all the samples is positive indicating holes as the dominant carrier for the thermally driven charge transport. For a 3D semiconductor, the diffusive component of the longitudinal thermopower follows the relation: $S_{xx}^{3D}(T) = m_d^* \frac{8\pi^2 k_B^2 T}{3eh^2} \left(\frac{\pi}{N}\right)^{2/3}$, where N = carrier concentration, m_d^* = effective mass, k_B = Boltzmann constant, e = electronic charge and h = Planck's constant [54]. We noticed that the value of S_{xx} increases with x for $x \leq 0.4$ but then decreases for $x = 0.5$. Most importantly, for all the samples, $S_{xx}(T)$ shows a broad maximum which shifts from $T_p \sim 150$ K for $x = 0$ to ~ 175 K for $x = 0.5$. Note that the peak in thermopower at low temperatures can arise due to the phonon-

1 drag or magnon-drag effects [55,56]. In a ferromagnetic conductor, electrons are scattered by
 2 spin waves, and this electron-magnon interaction is responsible for magnon-drag effect which
 3 is very similar to phonon-drag effect caused by electron-phonon scattering. While the
 4 contribution of phonon-drag effect in thermopower shows T^3 -dependence [55,56], the
 5 magnon-drag effect is closely related to the magnon specific heat and hence, it has the T -
 6 dependence of $T^{3/2}$ [55,57]. Therefore, we fitted our $S_{xx}(T)$ data for all the samples using the
 7 expression: $S_{xx}(T) = S_0 + S_d T + S_{mag} T^{3/2} + S_{ph} T^3 + S_{SW} T^4$; where, the second, third,
 8 fourth and fifth terms account for contributions from diffusion, magnon-drag effect, phonon-
 9 drag effect and spin-wave fluctuations, respectively [57,58]. The variations of the fitting
 10 parameters with Co doping are shown in **Fig. S5**. [32] It is evident that the absolute value of
 11 S_{mag} is ~ 4 orders of magnitude higher than that of S_{ph} , indicating dominant contribution of
 12 the magnon-drag effect. Note that, the phonon-drag effect induced maximum in $S_{xx}(T)$
 13 generally occurs around $T \approx (\theta_D/5)$ [56], where θ_D is the Debye temperature. Since θ_D was
 14 found to be ≈ 425 K for $\text{Co}_{1.1}\text{Fe}_{0.9}\text{GaCr}$ [29], the phonon-drag-driven maximum in $S_{xx}(T)$ is
 15 expected to occur ≈ 85 K. Since the broad maxima in $S_{xx}(T)$ occur at or above 150 K for all
 16 our samples, the magnon-drag effect is certainly the dominating mechanism for the broad peak
 17 and hence, for the thermoelectric transport in our $\text{Co}_{1+x}\text{Fe}_{1-x}\text{CrGa}$ system.

18



1

2 **Figure 4.** (a) Schematic illustration of ANE measurement on the $\text{Co}_{1+x}\text{Fe}_{1-x}\text{CrGa}$ samples.

3 Magnetic field dependence of the Nernst voltage, $V_{xy}(H)$ for different values of ΔT for (b) x

4 $= 0.0$ and (c) $x = 0.5$ at $T = 300\text{ K}$. (d) Normalized anomalous Nernst voltage, $S_{ANE} \times \Delta T =$

5 $V_{ANE}(\mu_0 H_{sat}) \times \left(\frac{L_z}{L_y}\right)$ as a function of ΔT showing linear ΔT -dependence.

6

7 Anomalous Nernst effect (ANE) measurements on the $\text{Co}_{1+x}\text{Fe}_{1-x}\text{CrGa}$ samples were

8 performed by sandwiching the samples between two copper blocks kept at different

9 temperatures, as shown in Fig. 4(a). A photograph of the actual set up along with the

10 measurement schematic is presented in Fig. S6. [32] A temperature gradient was applied along

11 the z -direction that generates a vertical temperature difference, $\Delta T = (T_{hot} - T_{cold})$ between

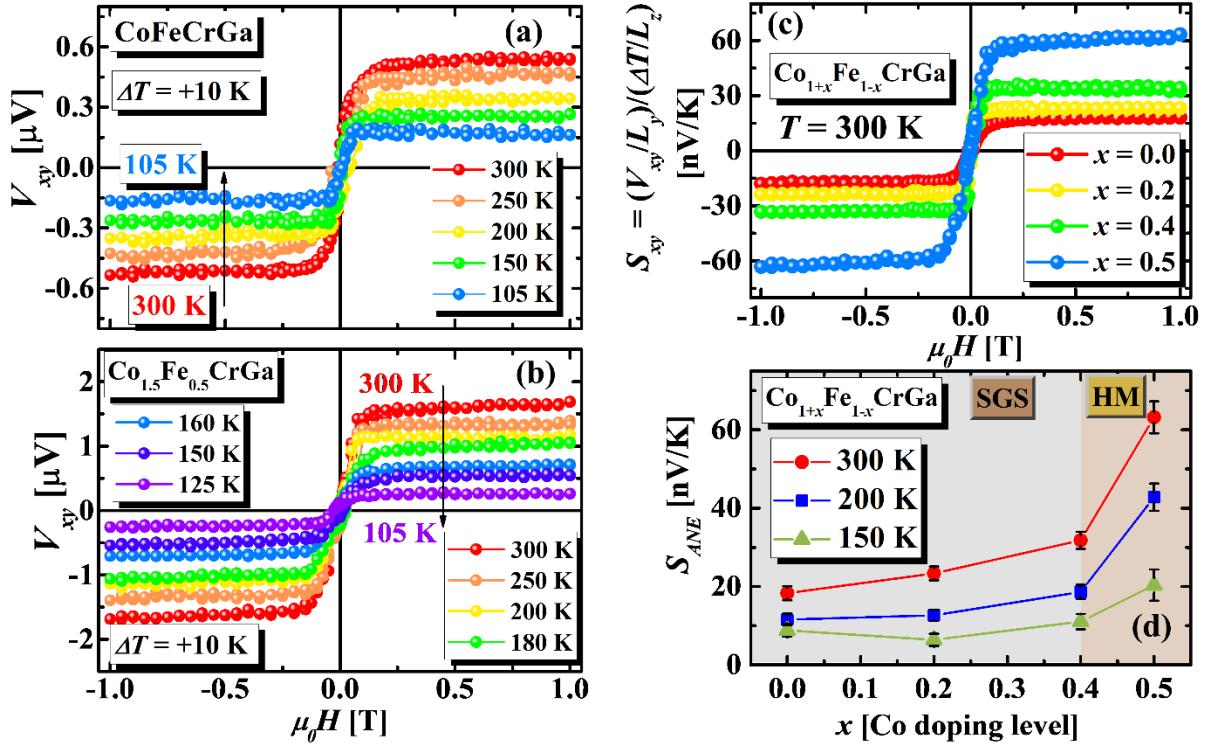
12 the bottom (hot) and top (cold) blocks that generates a transverse Nernst voltage along the y -

13 direction. In Fig. 4(b) and (c), we show the magnetic field dependence of the Nernst voltage,

14 $V_{xy}(H)$ for different values of ΔT for $x = 0.0$ and 0.5 in $\text{Co}_{1+x}\text{Fe}_{1-x}\text{CrGa}$, respectively at a

15 fixed temperature $T = \frac{T_{hot} + T_{cold}}{2} = 300\text{ K}$. The isothermal $V_{xy}(H)$ loops show negligible

1 hysteresis for all the samples, replicating their $M(H)$ behavior. It is clearly seen that the $V_{xy}(H)$
 2 signal strength increases with increasing the value of ΔT .
 3



4
 5 **Figure 5.** $V_{xy}(H)$ Hysteresis loops for (a) $x = 0.0$ and (b) $x = 0.5$ in $\text{Co}_{1+x}\text{Fe}_{1-x}\text{CrGa}$ at few
 6 selected temperatures for $\Delta T = +10$ K. (c) Comparison of the magnetic field dependence of the
 7 transverse Seebeck coefficient, $S_{xy}(H) = \frac{V_{xy}(H)}{\Delta T} \times \left(\frac{L_z}{L_y}\right)$ for all the samples in the series
 8 $\text{Co}_{1+x}\text{Fe}_{1-x}\text{CrGa}$ at $T = 300$ K for $\Delta T = +10$ K. (d) Comparison of the x -dependence of the
 9 background-corrected anomalous Nernst coefficient, $S_{ANE}(\mu_0 H_{sat}) = \frac{V_{ANE}(\mu_0 H_{sat})}{\Delta T} \times \left(\frac{L_z}{L_y}\right) =$
 10 $\frac{1}{2} \frac{[V_{xy}(+\mu_0 H_{sat}) - V_{xy}(-\mu_0 H_{sat})]}{\Delta T} \times \left(\frac{L_z}{L_y}\right)$ at $T = 300, 200$ and 150 K.

11
 12 In **Fig. 4(d)**, we present normalized anomalous Nernst voltage, $S_{ANE} \times \Delta T =$
 13 $V_{ANE}(\mu_0 H_{sat}) \times \left(\frac{L_z}{L_y}\right)$, as a function of ΔT for the samples $\text{Co}_{1+x}\text{Fe}_{1-x}\text{CrGa}$ at $T = 300$ K, where
 14 $V_{ANE}(\mu_0 H_{sat})$ is the background-corrected anomalous Nernst voltage defined
 15 as, $V_{ANE}(\mu_0 H_{sat}) = \left[\frac{V_{xy}(+\mu_0 H_{sat}) - V_{xy}(-\mu_0 H_{sat})}{2} \right]$, $\mu_0 H_{sat}$ is the saturation field, S_{ANE} is the

1 anomalous Nernst coefficient, L_y ($= 3$ mm for all the samples) is the separation between the
 2 voltage leads and L_z is the sample thickness along which the ΔT was applied. It is evident that
 3 $(S_{ANE} \times \Delta T)$ varies linearly with ΔT for all the samples, indicating intrinsic contribution of the
 4 thermally induced ANE signal [13,15].

5

6 **Fig. 5**(a) and (b) demonstrate the $V_{xy}(H)$ hysteresis loops for the samples $x = 0$ and 0.5
 7 in $\text{Co}_{1+x}\text{Fe}_{1-x}\text{CrGa}$, respectively at few selected temperatures for a fixed value of $\Delta T = +10$ K.

8 The $V_{xy}(H)$ hysteresis loops at different temperatures for the samples $x = 0.2$ and 0.4 are shown
 9 in the **Fig. S8**. [32] It is evident that the $V_{xy}(H)$ signal strength decreases with reducing

10 temperature. In **Fig. 5**(c), we compare the magnetic field dependence of the transverse Seebeck

11 coefficient, $S_{xy}(H)$ defined as, $S_{xy}(H) = \frac{V_{xy}(H)}{\Delta T} \times \left(\frac{L_z}{L_y}\right)$ for all the samples in the series

12 $\text{Co}_{1+x}\text{Fe}_{1-x}\text{CrGa}$ at $T = 300$ K for $\Delta T = +10$ K. Clearly, the $S_{xy}(H)$ signal increases with
 13 increasing Co doping (x). This is consistent with the fact that the thermally generated electric

14 field induced by ANE is proportional to the magnetization through the expression, [4,13]

15 $\vec{E}_{ANE} \propto (\mu_0 \vec{M} \times \vec{\nabla T})$ and, M_S of the samples $\text{Co}_{1+x}\text{Fe}_{1-x}\text{CrGa}$ also increases with x . In this

16 context, let us consider the contribution of the ordinary Nernst effect (NE) which is linearly

17 proportional to the applied magnetic field, $\vec{E}_{NE} \propto (\vec{H} \times \vec{\nabla T})$. The ordinary Nernst

18 contribution, S_{NE} was estimated from the slope of the slowly varying segment of the $S_{xy}(H)$

19 vs. H curves (*i.e.*, for $H \geq H_{sat}$) [13,15]. We found that $|S_{NE}| \approx 1.17 \times 10^{-4}$, 1.15×10^{-4} , $5.2 \times$

20 10^{-5} , and 7.6×10^{-4} nV. K⁻¹, for $x = 0, 0.2, 0.4$ and 0.5 respectively at $T = 300$ K. Therefore, the

21 ordinary NE contributes only $\approx 0.001\%$ of the total Nernst signal and hence, can be neglected,

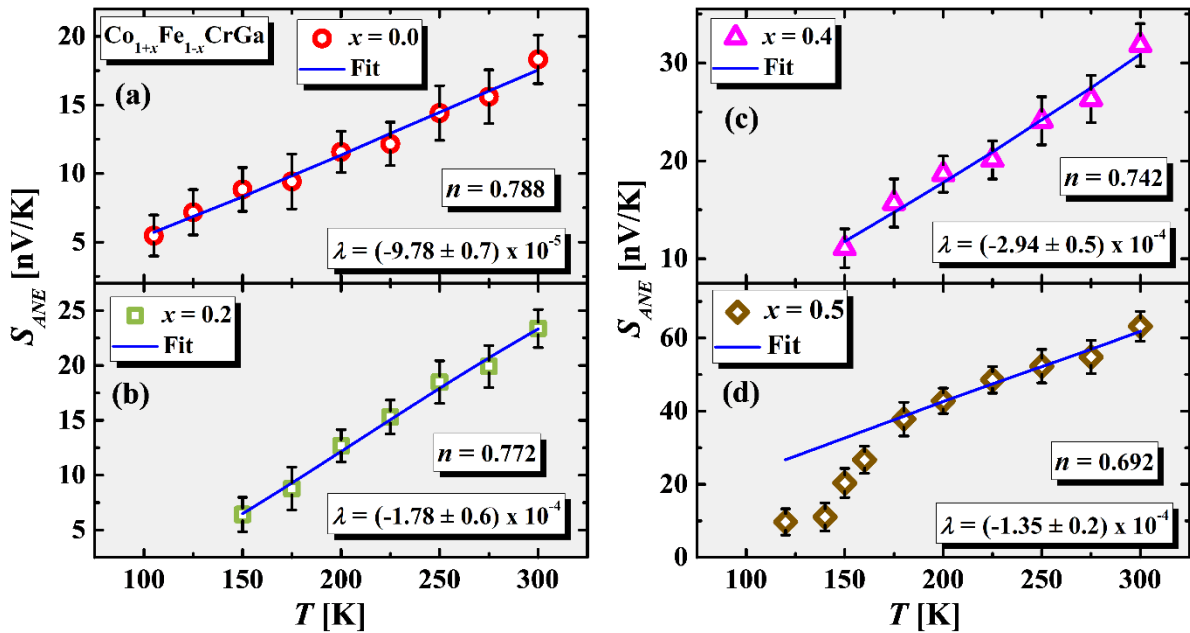
22 which indicates the dominant contribution of ANE in these samples. **Fig. 5**(d) compares the Co

23 doping level (x) dependence of the background-corrected anomalous Nernst coefficient,

24 $S_{ANE}(\mu_0 H_{sat}) = \frac{V_{ANE}(\mu_0 H_{sat})}{\Delta T} \times \left(\frac{L_z}{L_y}\right) = \frac{1}{2} \frac{[V_{xy}(+\mu_0 H_{sat}) - V_{xy}(-\mu_0 H_{sat})]}{\Delta T} \times \left(\frac{L_z}{L_y}\right)$ at $T = 300, 200$ and

1 150 K. It is evident that $S_{ANE}(\mu_0 H_{sat})$ increases slowly with x for $x \leq 0.4$ but rapidly between
 2 $x = 0.4$ and 0.5 (when it transforms from SGS state to completely half-metallic state), whereas
 3 M_S increases linearly with x which signifies that the ANE signal is not solely governed by the
 4 magnetization of the samples. The value of S_{ANE} for $x = 0.5$ at $T = 300$ K is $0.063 \mu\text{V} \cdot \text{K}^{-1}$
 5 which is higher than that for $\text{Ni}_{81}\text{Fe}_{19}$ ($0.048 \mu\text{V} \cdot \text{K}^{-1}$) [59] and compressively strained SrRuO_3
 6 films ($0.03 \mu\text{V} \cdot \text{K}^{-1}$) [60].

7



8

9 **Figure 6.** Temperature dependence of the anomalous Nernst coefficient $S_{ANE}(T)$ for (a) $x =$
 10 0.0 , (b) $x = 0.2$, (c) $x = 0.4$ and (d) $x = 0.5$ fitted with **Eqn. (1)**.

11

12 We show the temperature dependence of the anomalous Nernst coefficient $S_{ANE}(T)$ for
 13 the samples $x = 0, 0.2, 0.4$ and 0.5 in **Fig. 6**(a), (b), (c) and (d), respectively. Notably, $S_{ANE}(T)$
 14 for $x = 0$ decreases almost linearly with T in the temperature range, $105 \text{ K} \leq T \leq 300 \text{ K}$.
 15 However, for the samples $x = 0.2$ and 0.4 , we could get good ANE signal only up to 150 K ,
 16 and observed nearly T -linear behaviour in $S_{ANE}(T)$ for these two samples. Most interestingly,
 17 $S_{ANE}(T)$ for the sample $x = 0.5$ shows T -linear behaviour in the range: $200 \text{ K} \leq T \leq 300 \text{ K}$,

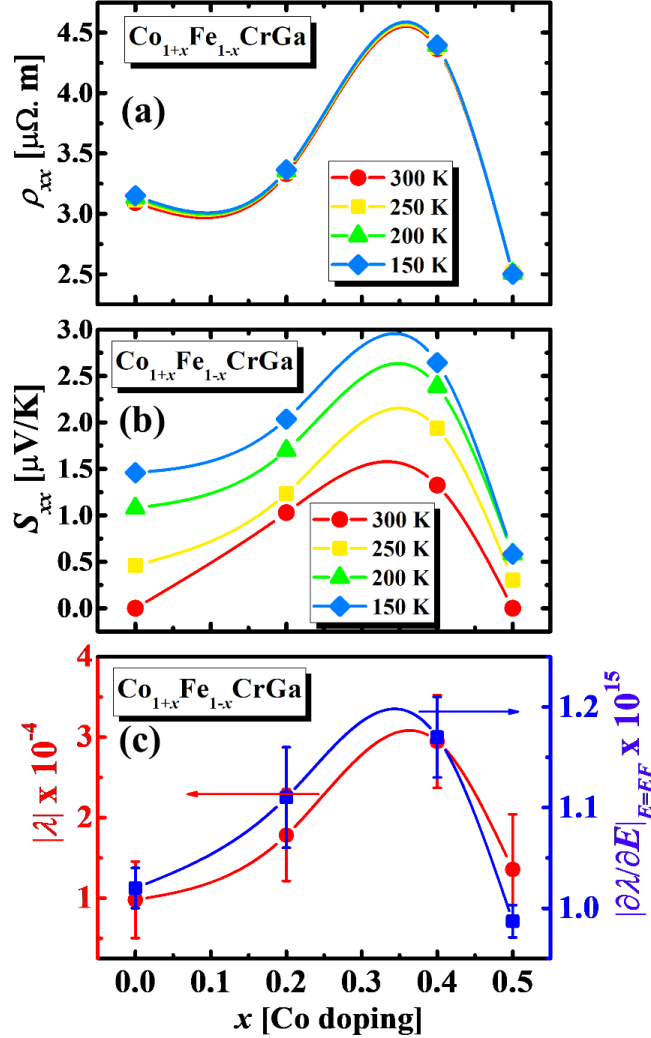
1 but undergoes a prominent slope change at 200 K followed by a nonlinear T -dependence which
2 is accompanied by a rapid decrease down to 125 K. In order to understand the underlying
3 mechanism for the observed behavior of $S_{ANE}(T)$ in the series $\text{Co}_{1+x}\text{Fe}_{1-x}\text{CrGa}$, let us begin
4 with the correlations among S_{xy} , S_{xx} , ρ_{xx} , and the transverse thermoelectric conductivity (the
5 Nernst conductivity) α_{xy} , which can be expressed as, $S_{xy} = \rho_{xx}(\alpha_{xy} - S_{xx}\sigma_{xy})$, where σ_{xy}
6 is the transverse electrical conductivity [13]. While S_{xx} is related to the energy derivative of
7 the longitudinal electrical conductivity, σ_{xx} at the Fermi level, E_F through the
8 expression [3,61]: $S_{xx} = \frac{\pi^2 k_B^2 T}{3e\sigma_{xx}} \left(\frac{\partial \sigma_{xx}}{\partial E} \right)_{E=E_F}$, α_{xy} is connected to the energy derivative of σ_{xy}
9 at E_F through the Mott's relation, [3] $\alpha_{xy} = \frac{\pi^2 k_B^2 T}{3e} \left(\frac{\partial \sigma_{xy}}{\partial E} \right)_{E=E_F}$. Let us recall the power law for
10 the anomalous Hall effect, which connects the transverse (ρ_{xy}) and the longitudinal resistivity
11 (ρ_{xx}) through the relation: $\rho_{xy} = \lambda \rho_{xx}^n$, where λ is the spin-orbit coupling constant.
12 Considering all the above-mentioned relations, S_{xy} can be expressed as, [3,13]

$$13 \quad S_{xy} = \rho_{xx}^{n-1} \left[\frac{\pi^2 k_B^2 T}{3e} \left(\frac{\partial \lambda}{\partial E} \right)_{E=E_F} - (n-1)\lambda S_{xx} \right] \quad (1)$$

14 Note that when $n = 1$, skew scattering is the dominating mechanism for the anomalous Nernst
15 transport and S_{xy} will be independent/weakly-dependent on the bulk electrical transport as well
16 as longitudinal thermoelectric properties of the material [62]. On the contrary, when $n = 2$, the
17 intrinsic Berry curvature or, the side jump is the dominating mechanism for the anomalous
18 Nernst transport [62]. Incorporating the $\rho_{xx}(T)$ and $S_{xx}(T)$ data, we fitted the $S_{ANE}(T)$ data
19 for our $\text{Co}_{1+x}\text{Fe}_{1-x}\text{CrGa}$ samples using **Eqn. (1)** taking λ , $\left(\frac{\partial \lambda}{\partial E} \right)_{E=E_F}$, and n as the fitting
20 parameter. We found that $S_{ANE}(T)$ for samples $x = 0 - 0.4$ fits well with the **Eqn. (1)** throughout
21 the measured temperature range, whereas that for $x = 0.5$ fits well only for $200 \text{ K} \leq T \leq$
22 300 K and deviates below 200 K. The value of n was found to decrease from 0.788 for $x = 0$ to

1 0.692 for $x = 0.5$ which signifies that the origin of ANE in the series $\text{Co}_{1+x}\text{Fe}_{1-x}\text{CrGa}$ is
 2 dominated by skew scattering mechanism [13–15,62].

3



4

5 **Figure 7.** The x -dependence of (a) ρ_{xx} and (b) S_{xx} at $T = 300, 250, 200$ and 150 K in $\text{Co}_{1+x}\text{Fe}_{1-x}$
 6 CrGa . (c) The x -dependence of $|\lambda|$ (left-y-axis) and $\left(\frac{\partial\lambda}{\partial E}\right)_{E=E_F}$ (right-y-axis).

7

8 We found that $|\lambda|$ increases from $(9.78 \pm 0.7) \times 10^{-5}$ for $x = 0$ to $(2.94 \pm 0.5) \times 10^{-4}$ for
 9 $x = 0.4$ but then decreases to $(1.35 \pm 0.6) \times 10^{-4}$ for $x = 0.5$. Moreover, the estimated values of

10 $\left(\frac{\partial\lambda}{\partial E}\right)_{E=E_F}$ for the samples $x = 0, 0.2, 0.4$ and 0.5 are $(1.02 \pm 0.02) \times 10^{15}$, $(1.11 \pm 0.05) \times 10^{15}$,

11 $(1.17 \pm 0.04) \times 10^{15}$ and, $(9.87 \pm 0.16) \times 10^{14}$, respectively. Note that the absolute values of both

1 $|\lambda|$ and $\left(\frac{\partial\lambda}{\partial E}\right)_{E=E_F}$ are quite close to those obtained for Fe_3O_4 single crystals [13]. It is known
2 that the Hall angle is related to λ and ρ_{xx} through the expression: $\tan \theta_{xy} = \frac{\sigma_{xy}}{\sigma_{xx}} = \frac{\lambda}{\rho_{xx}^{1-n}}$ [13].
3 Since $(1 - n) > 0$ for our $\text{Co}_{1+x}\text{Fe}_{1-x}\text{CrGa}$ samples, $\lambda \propto \rho_{xx}^{1-n}$, and hence the x -dependence of
4 $|\lambda|$ should follow the behavior of x -dependence of ρ_{xx} . Interestingly, as shown in [Fig. 7](#), the x -
5 dependence of both $|\lambda|$ and $\left(\frac{\partial\lambda}{\partial E}\right)_{E=E_F}$ for $\text{Co}_{1+x}\text{Fe}_{1-x}\text{CrGa}$ follow the trend of x -dependence of
6 ρ_{xx} as well as S_{xx} , indicating the significant role of longitudinal electrical and thermoelectric
7 transport properties in anomalous Nernst transport in this system. Our comprehensive studies
8 reported in this manuscript emphasize that there are several possibilities to enhance the
9 conversion efficiency of heat into Nernst thermopower by tuning the chemical composition of
10 SGSs and therefore, they can be very promising candidates for extremely tunable highly
11 efficient spin-caloritronics based device applications.

12

13 **4. Conclusions**

14 In summary, we present the first comprehensive investigation of the anomalous Nernst effect
15 in the quaternary Heusler alloy-based spin gapless semiconductors $\text{Co}_{1+x}\text{Fe}_{1-x}\text{CrGa}$. We found
16 that the electron-electron elastic scattering and the disorder mediated weak localization effect
17 play the major roles in electrical transport for all the samples at low temperatures, whereas the
18 magnon-drag effect is found to dominate the longitudinal thermoelectric transport. The ANE
19 coefficient, S_{ANE} increases slowly with x for $x \leq 0.4$ but rapidly between $x = 0.4$ and 0.5 , when
20 the system transforms from the SGS state to the completely half-metallic state. The value of
21 S_{ANE} for $x = 0.5$ at $T = 300$ K is $0.063 \mu\text{V} \cdot \text{K}^{-1}$ which is higher than that for $\text{Ni}_{81}\text{Fe}_{19}$ and
22 compressively strained SrRuO_3 films. Our analysis indicates that the observed ANE originates
23 from asymmetric skew-scattering of charge carriers.

24

1 **5. Acknowledgements**

2 Financial support by the US Department of Energy, Office of Basic Energy Sciences, Division
3 of Materials Science and Engineering under Award No. DE-FG02-07ER46438. HS also thanks
4 support from IIT Bombay for a short term visiting professorship.

5

6

7

8

9

10

11

12

13

14

15

16

17

18

19

20

21

22

23

24

25

1 **References**

- 2 [1] G. E. W. Bauer, E. Saitoh, and B. J. Van Wees, *Spin Caloritronics*, Nat. Mater. **11**,
3 391 (2012).
- 4 [2] M. Ikhlas, T. Tomita, T. Koretsune, M.-T. Suzuki, D. Nishio-Hamane, R. Arita, Y.
5 Otani, and S. Nakatsuji, *Large Anomalous Nernst Effect at Room Temperature in a*
6 *Chiral Antiferromagnet*, Nat. Phys. **13**, 1085 (2017).
- 7 [3] Y. Pu, D. Chiba, F. Matsukura, H. Ohno, and J. Shi, *Mott Relation for Anomalous Hall*
8 *and Nernst Effects in Ga 1- x Mn x As Ferromagnetic Semiconductors*, Phys. Rev.
9 Lett. **101**, 117208 (2008).
- 10 [4] A. Sakai, Y. P. Mizuta, A. A. Nugroho, R. Sihombing, T. Koretsune, M.-T. Suzuki, N.
11 Takemori, R. Ishii, D. Nishio-Hamane, R. Arita, and others, *Giant Anomalous Nernst*
12 *Effect and Quantum-Critical Scaling in a Ferromagnetic Semimetal*, Nat. Phys. **14**,
13 1119 (2018).
- 14 [5] H. Yang, W. You, J. Wang, J. Huang, C. Xi, X. Xu, C. Cao, M. Tian, Z.-A. Xu, J. Dai,
15 and others, *Giant Anomalous Nernst Effect in the Magnetic Weyl Semimetal Co 3 Sn 2*
16 *S 2*, Phys. Rev. Mater. **4**, 24202 (2020).
- 17 [6] L. Ding, J. Koo, L. Xu, X. Li, X. Lu, L. Zhao, Q. Wang, Q. Yin, H. Lei, B. Yan, and
18 others, *Intrinsic Anomalous Nernst Effect Amplified by Disorder in a Half-Metallic*
19 *Semimetal*, Phys. Rev. X **9**, 41061 (2019).
- 20 [7] A. Sakai, S. Minami, T. Koretsune, T. Chen, T. Higo, Y. Wang, T. Nomoto, M.
21 Hirayama, S. Miwa, D. Nishio-Hamane, and others, *Iron-Based Binary Ferromagnets*
22 *for Transverse Thermoelectric Conversion*, Nature **581**, 53 (2020).
- 23 [8] T. Chen, S. Minami, A. Sakai, Y. Wang, Z. Feng, T. Nomoto, M. Hirayama, R. Ishii,
24 T. Koretsune, R. Arita, and others, *Large Anomalous Nernst Effect and Nodal Plane in*
25 *an Iron-Based Kagome Ferromagnet*, Sci. Adv. **8**, eabk1480 (2022).

- 1 [9] D. Khadka, T. R. Thapaliya, S. H. Parra, J. Wen, R. Need, J. M. Kikkawa, and S. X.
2 Huang, *Anomalous Hall and Nernst Effects in Epitaxial Films of Topological Kagome*
3 *Magnet Fe₃Sn₂*, Phys. Rev. Mater. **4**, 84203 (2020).
- 4 [10] T. Asaba, V. Ivanov, S. M. Thomas, S. Y. Savrasov, J. D. Thompson, E. D. Bauer, and
5 F. Ronning, *Colossal Anomalous Nernst Effect in a Correlated Noncentrosymmetric*
6 *Kagome Ferromagnet*, Sci. Adv. **7**, eabf1467 (2021).
- 7 [11] Y. Pan, C. Le, B. He, S. J. Watzman, M. Yao, J. Gooth, J. P. Heremans, Y. Sun, and C.
8 Felser, *Giant Anomalous Nernst Signal in the Antiferromagnet YbMnBi₂*, Nat. Mater.
9 **21**, 203 (2022).
- 10 [12] J. Xu, W. A. Phelan, and C.-L. Chien, *Large Anomalous Nernst Effect in a van Der*
11 *Waals Ferromagnet Fe₃GeTe₂*, Nano Lett. **19**, 8250 (2019).
- 12 [13] R. Ramos, M. H. Aguirre, A. Anadón, J. Blasco, I. Lucas, K. Uchida, P. A. Algarabel,
13 L. Morellón, E. Saitoh, and M. R. Ibarra, *Anomalous Nernst Effect of Fe₃O₄ Single*
14 *Crystal*, Phys. Rev. B **90**, 54422 (2014).
- 15 [14] A. Ghosh, R. Das, and R. Mahendiran, *Skew Scattering Dominated Anomalous Nernst*
16 *Effect in La_{1-x}Na_xMnO₃*, J. Appl. Phys. **125**, 153902 (2019).
- 17 [15] A. Ghosh, A. Chanda, and R. Mahendiran, *Anomalous Nernst Effect in Pr_{0.5}Sr_{0.5}*
18 *CoO₃*, AIP Adv. **11**, 35031 (2021).
- 19 [16] A. Ghosh, A. Chanda, M. Manikandan, and R. Mahendiran, *Rare Earth Size*
20 *Dependence of Nernst Thermopower in Ferromagnetic Perovskites: R_{0.6}Sr_{0.4}CoO₃*
21 *(R= La, Pr, and Nd)*, J. Magn. Magn. Mater. **537**, 168240 (2021).
- 22 [17] T. Miyasato, N. Abe, T. Fujii, A. Asamitsu, S. Onoda, Y. Onose, N. Nagaosa, and Y.
23 Tokura, *Crossover Behavior of the Anomalous Hall Effect and Anomalous Nernst*
24 *Effect in Itinerant Ferromagnets*, Phys. Rev. Lett. **99**, 86602 (2007).
- 25 [18] X. L. Wang, *Proposal for a New Class of Materials: Spin Gapless Semiconductors*,

- 1 Phys. Rev. Lett. **100**, 156404 (2008).
- 2 [19] S. Ouardi, G. H. Fecher, C. Felser, and J. Kübler, *Realization of Spin Gapless*
3 *Semiconductors: The Heusler Compound Mn₂CoAl*, Phys. Rev. Lett. **110**, 100401
4 (2013).
- 5 [20] V. Alijani, J. Winterlik, G. H. Fecher, S. S. Naghavi, and C. Felser, *Quaternary Half-*
6 *Metallic Heusler Ferromagnets for Spintronics Applications*, Phys. Rev. B **83**, 184428
7 (2011).
- 8 [21] L. Bainsla, A. I. Mallick, M. M. Raja, A. K. Nigam, B. S. D. C. S. Varaprasad, Y. K.
9 Takahashi, A. Alam, K. G. Suresh, and K. Hono, *Spin Gapless Semiconducting*
10 *Behavior in Equiatomic Quaternary CoFeMnSi Heusler Alloy*, Phys. Rev. B **91**,
11 104408 (2015).
- 12 [22] L. Bainsla, A. I. Mallick, M. M. Raja, A. A. Coelho, A. K. Nigam, D. D. Johnson, A.
13 Alam, and K. G. Suresh, *Origin of Spin Gapless Semiconductor Behavior in*
14 *CoFeCrGa: Theory and Experiment*, Phys. Rev. B **92**, 45201 (2015).
- 15 [23] J. Hu, B. Ernst, S. Tu, M. Kuveždić, A. Hamzić, E. Tafra, M. Basletić, Y. Zhang, A.
16 Markou, C. Felser, and others, *Anomalous Hall and Nernst Effects in Co₂TiSn and*
17 *Co₂Ti_{0.6}V_{0.4}Sn Heusler Thin Films*, Phys. Rev. Appl. **10**, 44037 (2018).
- 18 [24] A. Ghosh, A. De, and S. Nair, *Large Anomalous Nernst Effect across the Magneto-*
19 *Structural Transition in a Bulk Ni-Co-Mn-Sn Full Heusler Alloy*, Appl. Phys. Lett.
20 **113**, 262405 (2018).
- 21 [25] J. Hu, T. Butler, M. A. Cabero Z, H. Wang, B. Wei, S. Tu, C. Guo, C. Wan, X. Han, S.
22 Liu, and others, *Regulating the Anomalous Hall and Nernst Effects in Heusler-Based*
23 *Trilayers*, Appl. Phys. Lett. **117**, 62405 (2020).
- 24 [26] C. D. W. Cox, A. J. Caruana, M. D. Cropper, and K. Morrison, *Anomalous Nernst*
25 *Effect in Co₂MnSi Thin Films*, J. Phys. D: Appl. Phys. **53**, 35005 (2019).

- 1 [27] Y. Sakuraba, K. Hyodo, A. Sakuma, and S. Mitani, *Giant Anomalous Nernst Effect in*
2 *the Co₂MnAl_{1-x}Si_x Heusler Alloy Induced by Fermi Level Tuning and Atomic*
3 *Ordering*, Phys. Rev. B **101**, 134407 (2020).
- 4 [28] A. De, A. K. Singh, S. Singh, and S. Nair, *Temperature Dependence of the Anomalous*
5 *Nernst Effect in Ni₂MnGa Shape Memory Alloy*, Phys. Rev. B **103**, L020404 (2021).
- 6 [29] D. Rani, L. Bainsla, K. G. Suresh, A. Alam, and others, *Spin-Gapless Semiconducting*
7 *Nature of Co-Rich Co_{1+x}Fe_{1-x}CrGa*, Phys. Rev. B **99**, 104429 (2019).
- 8 [30] A. Chanda, C. Holzmann, N. Schulz, J. Seyd, M. Albrecht, M.-H. Phan, and H.
9 Srikanth, *Scaling of the Thermally Induced Sign Inversion of Longitudinal Spin*
10 *Seebeck Effect in a Compensated Ferrimagnet: Role of Magnetic Anisotropy*, Adv.
11 *Funct. Mater.* **32**, 2109170 (2022).
- 12 [31] A. Chanda, D. DeTellem, Y. T. Hai Pham, J. E. Shoup, A. T. Duong, R. Das, S. Cho,
13 D. V. Voronine, M. T. Trinh, D. A. Arena, and others, *Spin Seebeck Effect in Iron*
14 *Oxide Thin Films: Effects of Phase Transition, Phase Coexistence, and Surface*
15 *Magnetism*, ACS Appl. Mater. Interfaces **14**, 13468 (2022).
- 16 [32] See Supplemental Material at [\[link\]](#) for Additional Transport Data.
- 17 [33] J. Nag, D. Rani, D. Singh, R. Venkatesh, B. Sahni, A. K. Yadav, S. N. Jha, D.
18 Bhattacharyya, P. D. Babu, K. G. Suresh, and others, *CoFeVSb: A Promising*
19 *Candidate for Spin Valve and Thermoelectric Applications*, Phys. Rev. B **105**, 144409
20 (2022).
- 21 [34] A. C. Anderson, R. B. Rauch, and M. M. Kreitman, *Another Comparison of Thermal*
22 *Bonding Agents*, Rev. Sci. Instrum. **41**, 469 (1970).
- 23 [35] E. Gmelin, M. Asen-Palmer, M. Reuther, and R. Villar, *Thermal Boundary Resistance*
24 *of Mechanical Contacts between Solids at Sub-Ambient Temperatures*, J. Phys. D.
25 *Appl. Phys.* **32**, R19 (1999).

- 1 [36] B. Shi, J. Li, C. Jin, J. Yang, C. Zhang, Y. Yan, Y. Wang, and G. Zhang, *Distinct*
2 *Transport Behaviors and Electronic Structures in Heusler Alloys CoFeCrGa and*
3 *CoFeCrAl*, J. Magn. Mater. **517**, 167383 (2021).
- 4 [37] I. Galanakis, P. H. Dederichs, and N. Papanikolaou, *Slater-Pauling Behavior and*
5 *Origin of the Half-Metallicity of the Full-Heusler Alloys*, Phys. Rev. B **66**, 174429
6 (2002).
- 7 [38] D. S. Rana, J. H. Markna, R. N. Parmar, D. G. Kuberkar, P. Raychaudhuri, J. John, and
8 S. K. Malik, *Low-Temperature Transport Anomaly in the Magnetoresistive Compound*
9 *(La 0.5 Pr 0.2) Ba 0.3 MnO 3*, Phys. Rev. B **71**, 212404 (2005).
- 10 [39] P. A. Lee and T. V Ramakrishnan, *Disordered Electronic Systems*, Rev. Mod. Phys.
11 **57**, 287 (1985).
- 12 [40] C. Cirillo, C. Barone, H. Bradshaw, F. Urban, A. Di Bernardo, C. Mauro, J. W. A.
13 Robinson, S. Pagano, and C. Attanasio, *Magnetotransport and Magnetic Properties of*
14 *Amorphous $\backslash\mathrm{\$}\{\$NdNi\}\$ _5 \$ NdNi 5 Thin Films$* , Sci. Rep.
15 **10**, 1 (2020).
- 16 [41] D. Gnida, K. Ciesielski, and D. Kaczorowski, *Origin of the Negative Temperature*
17 *Coefficient of Resistivity in the Half-Heusler Antimonides LuNiSb and YPdSb*, Phys.
18 Rev. B **103**, 174206 (2021).
- 19 [42] J. Kondo, *Resistance Minimum in Dilute Magnetic Alloys*, Prog. Theor. Phys. **32**, 37
20 (1964).
- 21 [43] A. N. Pasupathy, R. C. Bialczak, J. Martinek, J. E. Grose, L. A. K. Donev, P. L.
22 McEuen, and D. C. Ralph, *The Kondo Effect in the Presence of Ferromagnetism*,
23 Science (80-.). **306**, 86 (2004).
- 24 [44] J. Zhang, Y. Xu, S. Cao, G. Cao, Y. Zhang, and C. Jing, *Kondo-like Transport and Its*
25 *Correlation with the Spin-Glass Phase in Perovskite Manganites*, Phys. Rev. B **72**,

- 1 54410 (2005).
- 2 [45] S. Chatterjee, S. Chatterjee, S. Giri, and S. Majumdar, *Transport Properties of Heusler*
3 *Compounds and Alloys*, J. Phys. Condens. Matter (2021).
- 4 [46] K. Yamada, M. Nakano, K. Yoshida, K. Hanzawa, and A. Sakurai, *T-Square Term of*
5 *Electrical Resistivity*, Prog. Theor. Phys. **82**, 689 (1989).
- 6 [47] A. Urushibara, Y. Moritomo, T. Arima, A. Asamitsu, G. Kido, and Y. Tokura,
7 *Insulator-Metal Transition and Giant Magnetoresistance in $La_{1-x}Sr_xMnO_3$* , Phys.
8 Rev. B **51**, 14103 (1995).
- 9 [48] D. Kim, Q. Li, P. Syers, N. P. Butch, J. Paglione, S. Das Sarma, and M. S. Fuhrer,
10 *Intrinsic Electron-Phonon Resistivity of Bi_2Se_3 in the Topological Regime*, Phys.
11 Rev. Lett. **109**, 166801 (2012).
- 12 [49] A. W. Forbes, R. P. Dulal, N. Bhattarai, I. L. Pegg, and J. Philip, *Experimental*
13 *Realization and Magnetotransport Properties of Half-Metallic Fe_2Si* , J. Appl. Phys.
14 **125**, 243902 (2019).
- 15 [50] D. Bombor, C. G. F. Blum, O. Volkonskiy, S. Rodan, S. Wurmehl, C. Hess, and B.
16 Büchner, *Half-Metallic Ferromagnetism with Unexpectedly Small Spin Splitting in the*
17 *Heusler Compound Co_2FeSi* , Phys. Rev. Lett. **110**, 66601 (2013).
- 18 [51] A. Barry, J. M. D. Coey, L. Ranno, and K. Ounadjela, *Evidence for a Gap in the*
19 *Excitation Spectrum of CrO_2* , J. Appl. Phys. **83**, 7166 (1998).
- 20 [52] Y. Xu, J. Zhang, G. Cao, C. Jing, and S. Cao, *Low-Temperature Resistivity Minimum*
21 *and Weak Spin Disorder of Polycrystalline $La_{2/3}Ca_{1/3}MnO_3$ in a Magnetic*
22 *Field*, Phys. Rev. B **73**, 224410 (2006).
- 23 [53] D. Rani, J. Kangsabanik, K. G. Suresh, N. Patra, D. Bhattacharyya, S. N. Jha, and A.
24 Alam, *Origin of Local Atomic Order and Disorder in $Co_2Fe_{1-x}Cr_xSi$ Heusler*
25 *Alloys: Theory and Experiment*, Phys. Rev. Appl. **10**, 54022 (2018).

- 1 [54] J. P. Heremans, V. Jovovic, E. S. Toberer, A. Saramat, K. Kurosaki, A.
2 Charoenphakdee, S. Yamanaka, and G. J. Snyder, *Enhancement of Thermoelectric*
3 *Efficiency in PbTe by Distortion of the Electronic Density of States*, Science (80-.).
4 **321**, 554 (2008).
- 5 [55] P. Mandal, *Temperature and Doping Dependence of the Thermopower in LaMnO₃*,
6 Phys. Rev. B **61**, 14675 (2000).
- 7 [56] J. Yang, Y. P. Sun, W. H. Song, and Y. P. Lee, *Thermopower and Thermal*
8 *Conductivity of the Electron-Doped Manganite La_{0.9}Te_{0.1}MnO₃*, J. Appl. Phys.
9 **100**, 123701 (2006).
- 10 [57] A. Banerjee, S. Pal, S. Bhattacharya, B. K. Chaudhuri, and H. D. Yang,
11 *Magnetoresistance and Magnetothermoelectric Power of La_{0.5}Pb_{0.5}Mn_{1-x}Cr_xO₃*,
12 Phys. Rev. B **64**, 104428 (2001).
- 13 [58] R. Das, A. Chanda, and R. Mahendiran, *Influence of Magnetic Field on Electrical and*
14 *Thermal Transport in the Hole Doped Ferromagnetic Manganite: La_{0.9}Na_{0.1}MnO₃*,
15 RSC Adv. **9**, 1726 (2019).
- 16 [59] J. Holanda, O. A. Santos, R. O. Cunha, J. B. S. Mendes, R. L. Rodr\iguez-Suárez, A.
17 Azevedo, and S. M. Rezende, *Longitudinal Spin Seebeck Effect in Permalloy*
18 *Separated from the Anomalous Nernst Effect: Theory and Experiment*, Phys. Rev. B
19 **95**, 214421 (2017).
- 20 [60] D. Kan and Y. Shimakawa, *Strain Effect on Thermoelectric Properties of SrRuO₃*
21 *Epitaxial Thin Films*, Appl. Phys. Lett. **115**, 22403 (2019).
- 22 [61] N. F. Mott, H. Jones, H. Jones, and H. Jones, *The Theory of the Properties of Metals*
23 *and Alloys* (Courier Dover Publications, 1958).
- 24 [62] N. Nagaosa, J. Sinova, S. Onoda, A. H. MacDonald, and N. P. Ong, *Anomalous Hall*
25 *Effect*, Rev. Mod. Phys. **82**, 1539 (2010).